IEEE Access
Multidisciplinary ⋮ Rapid Review ⋮ Open Access Journal

Received 26 June 2025, accepted 18 July 2025, date of publication 23 July 2025, date of current version 30 July 2025.

Digital Object Identifier 10.1109/ACCESS.2025.3591959

RESEARCH ARTICLE

WISP: Workframe for Interferogram Signal Phase-Unwrapping

TIMOFEY F. KHIRIANOV[1,2], **ALEKSANDRA I. KHIRIANOVA**[2], **EGOR V. PARKEVICH**[2], **AND ILYA MAKAROV**[1,3,4,5]

[1]Moscow Institute of Physics and Technology, 141701 Dolgoprudny, Russia
[2]Lebedev Physical Institute of the Russian Academy of Sciences, 119991 Moscow, Russia
[3]AIRI, 105064 Moscow, Russia
[4]ISP RAS, 109004 Moscow, Russia
[5]Artificial Intelligence Research Center, National Research Nuclear University MEPhI, 115409 Moscow, Russia

Corresponding author: Timofey F. Khirianov (khirianov.tf@mipt.ru)

The work was supported by a grant for research centers in the field of artificial intelligence provided by the Ministry of Economic Development of the RF under the subsidy agreement (agreement identifier 000000C313925P3Q0002) with National Research Nuclear University MEPhI No. 70-2023-001309.

ABSTRACT This paper proposes an iterative framework WISP (Workframe for Interferogram Signal Phase-unwrapping for phase reconstruction from interferograms of complex phase objects. The framework processes each interferogram through the sequential stages: dark fringe tracing, isophase distribution, local gradient direction estimation, anisotropic (local direction dependent) diffusion smoothing, phase unwrapping, and convergence testing. Iterations continue until the difference between the reconstructed and experimental phase distributions reaches an asymptotic minimum. A key contribution is the proposed loss function for isophase fitting, which directly optimizes curve quality and enhances reconstruction accuracy. Experimental results confirm the algorithm's highest precision. A study of the framework's resistance to noise was conducted, showing high stability even in the case of noise with an amplitude half the amplitude of the image brightness. Comparative analysis against established baselines reveals that the WISP consistently outperforms alternative approaches in accurately unwrapping the phase, particularly under high noise conditions. Evaluated using RMSD metrics, WISP achieves the lowest reconstruction errors, reducing them by 39.7% compared to the next best method (Deep Convolutional Neural Network), highlighting its superior robustness and accuracy.

INDEX TERMS Phase unwrapping, fringe tracing, optical systems, computational imaging, adaptive optics.

I. INTRODUCTION

Laser interferometry is a fundamental technique for measuring the density of transparent objects. Interferograms encode complex interference patterns that reveal the spatial distribution of the refractive index of an object. The accuracy of retrieving this information depends both on the quality of the raw data and the interferogram analysis method.

To reconstruct the optical density, the phase distribution of the interference pattern must be determined with high precision. However, this task is challenging due to the noise, complex fringe morphologies, and limitations of existing phase extraction techniques.

Our research group developed the Parabola Method (PM) [1], which is a robust approach for tracing dark fringes with high precision. The phase reconstruction between the fringes was achieved through geometric interpolation. PM successfully processes interferograms with oscillatory inflections while preserving fringe sharpness and resolution, enabling studies of complex plasma morphologies in spark discharges (see [3], [4], [5]).

Similar to other ridge-tracing methods, PM exhibits sensitivity to high-frequency speckle noise present in the imagery, which can be mitigated through preliminary Fourier filtering techniques. Nevertheless, the principal challenge in

The associate editor coordinating the review of this manuscript and approving it for publication was Joewono Widjaja.

analyzing our specific phase objects was the manifestation of interference fringes with negative curvature, which the PM could not process. An additional limitation lies in the geometric computation of intermediate isophases that frequently deviate from actual physical conditions. Consequently, this necessitates disregarding brightness distributions between the dark fringe patterns.

Because the parabola method proved to be inapplicable in these cases, we adopted the Extended Approach Parabola Method (EAPM) [2], which demonstrated significant improvements over conventional PM. During the implementation of the EAPM, we encountered two fundamental problems: the substantial computational complexity of the method and systematic accumulation of errors across iterations. The computational complexity was successfully addressed using optimized CPython implementation and concurrent programming techniques. However, the phase reconstruction errors persisted as they were inherently linked to the PM's core methodology. Reliable prediction of line spatial frequencies requires smoothed images, while effective smoothing necessitates curve windows aligned with fringe directions, which in turn cannot be accurately determined without prior knowledge of spatial frequencies. This circular dependency creates an inescapable limitation, highlighting the need for alternative interferogram processing algorithms capable of extracting phase shift information with reliable accuracy under such conditions.

In this article, we present a new iterative phase unwrapping framework WISP (Workframe for Interferogram Signal Phase-unwrapping) that includes **PM-based initial isophase determination** and an **iterative refinement procedure** designed to enhance reconstruction accuracy. The refinement process consists of the following components:

- Positional **refinement of dark fringes and isophases** using original loss-based tuning approach,
- Dynamic **recomputation of directional field** using updated information about isophases;
- **Anisotropic image smoothing** and noise filtering;
- Dynamic **recomputation of gradient field** using updated information about phase and, as a result, changed isophases;
- **Phase reconstruction** with our novel tuning methodology;
- Precision-based iteration **termination criteria** relying on the absence of significant changes between iterations in the accuracy of the reconstructed phase matching the experimental image.

This comprehensive framework delivers reliable results even when processing highly noisy interferograms (the relevant research is presented in SectionV) exhibiting complex fringe behavior.

We quantitatively compare our WISP framework's phase reconstruction accuracy against established baselines, including the reliability-guided fast non-continuous path (RFNP) algorithm [6], [7], transport-of-intensity equation (TIE) and its iterative variant (ITIE) [8], the original PM [1], its extended version EAPM [2] and deep convolutional neural network approaches (DCNN) [9].

The comparative accuracy assessment revealed that the WISP method achieves superior performance in matching the interference function derived from the reconstructed phase data with the original frames, particularly under noisy conditions. Quantitative evaluation using the root mean square deviation (RMSD) metric demonstrated that our framework consistently outperforms all benchmarked methods, maintaining the lowest error values across varying noise levels. The advantage of RMSD was most pronounced in the high-noise regime, where WISP reduced reconstruction errors by 39.7% compared to the next-best-performing method (DCNN). These results demonstrate that WISP achieves superior robustness and accuracy in diverse morphologies of interference patterns.

The **key contributions** of this work can be summarized as follows:

- Development of an **innovative adaptive trace correction methodology** that enables precise positional refinement of both dark fringes and isophases through our original loss-based optimization method.
- Introduction of an **anisotropic filtering along the local fringe orientation algorithm** that selectively preserves the fringe morphology while effectively suppressing high-frequency noise components.
- Formulation of a **novel iterative phase reconstruction framework** incorporating precision-based **termination criteria** for achieving absence of significant changes in the precision of compliance with the experiment.

II. RELATED WORK

The well-known and reliable methods for high-precision phase retrieval are the temporal phase-shifting technique [10], [11], [12] and parallel phase-shifting [13], [14].

However, in the case of ultrafast processes, when only a single fringe pattern image can be captured, the conventional phase-shifting methods cannot be applied directly. This limitation arises because temporal phase scanning requires multiple frames with known phase shifts for accurate reconstruction of phase information. Parallel phase shifting assumes registration of several images by one camera, which requires precise measurement of optical paths and fine adjustment, potentially decreasing the final image size.

For such processes, alternative methods exist for extracting phase information from a single fringe pattern image: windowed Fourier transform (WFT) [15], [16], [17], [18], continuous wavelet transform (CWT) [20], [21], [22], Hilbert-Huang transform-based methods [23], [24], [25].

WFT as well known as the Short-Time Fourier Transform applies a sliding window to a fringe pattern and performs Fourier analysis on localized regions [18]. The method's performance critically depends on the chosen window size. It is a fundamental trade-off between spatial and frequency resolution. Smaller windows give better spatial localization but worse frequency resolution. Since Fourier transform calculation is required for each window position, the WFT method is computationally intensive [15]. Additional limitations include high sensitivity to noise and inhomogeneities, boundary effects, and the need for careful, often manual selection of window parameters [15].

The work [19] presents an algorithm that combines recent advances in smoothing and leveling preprocessing with Fourier transform analysis with perfect results.

The WISP framework employs anisotropic smoothing guided by local fringe directionality and gradient analysis to achieve automated, artifact-free noise suppression while preserving boundary integrity without manual parameter tuning.

Hilbert-Huang transform applied to 2D images is called Bidirectional Empirical Mode Decomposition (BEMD). Unlike WFT and CWT, it does not use the presumed decomposition basis; the basis is derived from the signal itself through characteristic intrinsic mode functions. The method shows better accuracy results than WFT [23], but the practical usage of BEMD is limited by the calculation time. Fast Adaptive Bidirectional Empirical Mode Decomposition [25], which claims improved results with the reduced algorithmic complexity, remains relatively resource-intensive. Since the algorithm does not have a strict mathematical justification, the selection of parameters for the correct restoration of phase information requires additional analysis and an expert approach [25].

WISP avoids eliminating basic signal components that could unpredictably distort quantitative characteristics of the studied object. It also includes a numerical estimate of the deviation error from the original pattern.

In recent years, deep learning methods for phase reconstruction have emerged. Having been trained properly, neural networks can perform fast and robust phase unwrapping in just one step [26]. Modern algorithms like Deep Learning Phase Unwrapping show promising results [26], [27], [28], [29].

Since interferograms are primarily images, the preferential use of convolutional neural networks (CNNs), which are optimally designed for image processing, is natural [29]. In [26], a CNN with a U-Net-like architecture is used to process interferograms.

The work [27] proposes a comprehensive approach that combines interferogram predenoising and phase extraction. Specifically, a cascaded CNN architecture is utilized: initially, a Denoising CNN module denoises the wrapped phase, followed by a U-Net that performs phase unwrapping.

In [28], a hybrid network that combines CNN and components of the recurrent neural network is applied. CNN extracts spatial features, while recurrent layers capture temporal dependencies across sequences of phase images. In the work [30] the combination of CNN with self-attention mechanism is used.

In phase reconstruction, deep learning methodologies aim to automatically determine relationships between data through optimization of neural network parameters on empirical datasets. Neural networks, with their multilayered architecture and millions of adjustable parameters, demonstrate the capacity to capture complex dependencies. However, unlike physics-based algorithms, generalized neural network structures frequently exhibit opacity; it remains challenging to discern precisely what the network has learned and what function a specific parameter performs. This opacity presents significant challenges when neural network failures occur: it becomes impossible to analyze the underlying cause of the failure or implement targeted improvements to prevent similar errors in subsequent applications.

Moreover, the other disadvantage is the need for large labeled data for training. The lack of correctly processed experimental data of the type of frames under study is a well-known problem among researchers.

WISP offers parametric transparency regarding noise and artifact elimination, the scale and degree of impact on the original pattern during processing, and a clear mathematical criterion for compliance with the original experimental image.

Due to these considerations, traditional regularized phase tracking (RPT) methods continue to be widely used worldwide, particularly in cases requiring expert evaluation of results. Empirical studies demonstrate the relevance and competitiveness of RPT methods [31], [32], [33].

III. FRAMEWORK OVERVIEW

Considering the main problems of the EAPM method, which introduces additional changes to the frame patterns under investigation in each processing iteration, we decided to abandon this type of iterative frame processing and instead focused on iterative refinement of phase parameters at each point (pixel) of the frame.

For a further detailed description of the method, we need to make several assumptions and introduce the necessary terminology.

A. ASSUMPTIONS

First, we assume that the true (noise-free) phase distribution in the two-dimensional frame space (height, width) and its first derivatives with respect to coordinates are continuous along both coordinates.

This assumption is justified first by the **mathematical correctness** of the problem of reconstructing the phase distribution in the frame from an interference pattern. If we were to assume the possibility of discontinuities in the two-dimensional phase distribution, its correct reconstruction from a single frame would become impossible (for example, a phase jump of 2π is not detectable in an interference frame).

Secondly, this assumption is related to the **physical plausibility**. The structure of the recorded objects, where the continuity of density parameters and consequently optical permeability, is often a continuous quantity. This results in a continuous interference pattern.

The mathematical notations given here and below are collected for convenience in Table3 in AppendixB.

There is a fundamental basis for such assumptions. The differential form of Maxwell's equations expresses at every point in space and moment in time the relationships between field vectors and current densities. For these equations to hold true, it is assumed that the field vectors are single-valued, finite, and continuous functions with continuous derivatives with respect to position [34].

Assuming the continuity of the phase function $\phi(x, y)$, we can implement a transition to the gradient vector $\nabla\phi(x, y)$, which expresses the direction of the most rapid phase increase at point (x, y).

Furthermore, we will use the concept of **isophase** - a line connecting the nearest points with equal phases. In our problem formulation, we will consider characteristic forms of interferograms that do not have isophase discontinuities or closed isophases. From the definition of the gradient, the tangent to the isophase at each point is perpendicular to the vector $\nabla\phi(x, y)$.

Additionally, phase **gradient** lines - lines whose tangents coincide with the direction of the phase gradient, will also be continuous because of the continuity of the phase function and its first derivatives with respect to the coordinates. Furthermore, these lines cannot exhibit self-intersections or mutual intersections. Both of these assertions follow from Picard's theorem. If the partial derivatives of a function satisfy the Lipschitz condition, then a unique gradient line passes through each point.

Critical points (centers of closed lines and saddle points) will remain outside the scope of this methodology; however, it is worth mentioning that the processing of critical points represents a direction for future work of the authors.

B. FRAMEWORK STRUCTURE

Similar to most classical interferometry processing methods, our method is iterative, but with an important significant amendment: no iterative changes are made to the original frame. The framework scheme is shown in Figure 1.

The diagram illustrates key components: initial fringe pre-tracing with iterative line tuning via a novel loss SKIM-function, geometrical isophase construction, direction calculation, anisotropic smoothing, gradient lines construction, phase unwrapping, and re-tracing with SKIM-based isophase tuning in case of entering a new cycle. The iterations stopping condition of reaching an asymptotic minimum of the difference with experimental data ensures robust convergence and prevents unnecessary computation.

First, prior to the initial iteration, a **preliminary tracing** method for brightness minimum fringes is implemented. Brightness minimum lines are the isophases corresponding to lines with minimal brightness in the frame, or black fringes. Such tracing methods are well-established and thoroughly documented ([31], [32], [33]). In our case, the implementation was based on the parabola method ([1], [2]) and is briefly described in Subsection IV-A.

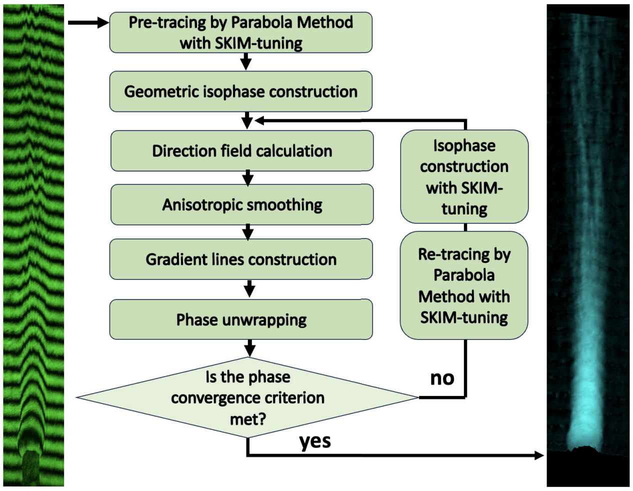

FIGURE 1. Schematic representation of the iterative phase reconstruction process.

Then, this initial position of the **dark fringes** is **adjusted**, improving the quality of its construction. To measure the quality of the black stripe construction, we introduce a **novel loss function** - Smoothed Kernel-based Intensity Measuring (SKIM) function. The minimization of this metric is performed using the gradient loss minimization method. This method can be applied to any primary tracing principle to improve its precision. Formula specifics concerning the SKIM function in the loss paradigm as well as the minimization procedure are described in detail in Subsection IV-B.

Then, a series of isophase lines is constructed between the black fringes. The mechanism for **constructing isophases** during the first iteration is **geometric** and is described in Subsection IV-C, while subsequent iterations will rely on adaptively obtained data regarding the presumed phase distribution in the frame.

Then, on the basis of the isophases obtained, the **local direction field, or the map of angle distribution** of the isophase is calculated to correct for the smoothing of the interference frame along the presumed lines of constant phase incursion. This algorithm is described in Subsection IV-D.

Subsequently, we apply **anisotropic diffusion smoothing** to the intensity pattern along the isophase lines. The smoothing in each iteration operates on the original image rather than the result of the previous iteration, avoiding progressive blurring and preserving the curvature of the line bends. This ensures reliable fringe pattern processing, as detailed in Subsection IV-E.

Separately from the previous two stages, using only isophase lines, we trace continuous **phase gradient lines** (orthogonal to the isophases). Their presence reduces the phase reconstruction problem from a two-dimensional to a one-dimensional task. The method for constructing these continuous, non-intersecting lines is detailed in Subsection IV-F.

For pixels along a gradient line, the brightness of the recorded (and smoothed) interference pattern provides the reference data needed to **reconstruct phase values**, using a novel loss-based optimization method to adjust constant-phase line positions. This tuning process is described in detail in Subsection IV-G.

The two-dimensional phase distribution of all gradient lines **recalculates the dark lines and isophases**, which then serve as input for the next iteration. This stage is detailed in Section IV-H. The adaptive isophase construction method is an original contribution of this work.

The method then iteratively repeats these stages for each frame. Iterations are terminated when the difference between the experimental frame and the interference function (derived from the reconstructed phase distribution) reaches an asymptotic minimum. This **stopping criterion** is briefly outlined in Section IV-I and was originally introduced in [35].

We also provide algorithmic pseudocode A showing which data is used and passed through each stage of the framework.

IV. FRAMEWORK ALGORITHMS

For clarity of presentation, we will give an example of step-by-step processing of an interferogram frame (see Fig. 2(a)). This shift interferogram was obtained from the experimental setup [36], which studied the formation of highly ionized plasma channels during nanosecond discharges in atmospheric air. The plasma channel was probed with a 70 ps laser pulse (532 nm wavelength). The image was taken with a 10x magnification on the CMOS matrix of a Canon1200 camera, which achieves a frame resolution of 3 pixels, or 5 μm. Plasma channel diameter was 120-140 μm.

The near-cathode zone appears as a monostructure, while upper regions show intensity bursts, density filaments with transverse dimensions of the order of 10-20 μm.

The complexity of the phase object lies primarily in the presence of complex bends of lines with sharp angles in the filamentation region, close in spatial scale to noise, band broadening and artifacts, and the need to extract physically plausible phase information about the filamentated object from the interference frame. High-quality tracing of these filaments represent a challenge in processing this frame.

A. PRE-TRACING

In the first stage, tracing, or construction of connected numbered black lines for dark fringes in an interference frame is performed using the PM. The algorithm was detailed in work [1], and its essence is **to determine** points (pixels) - **candidates** for belonging to black lines according to the following principle. A slice of image intensities is taken with the center at the point under investigation, and a parabola is constructed that optimally approximates this intensity slice, with its vertex at the investigated point. For each point, the root mean square deviation of the slice from the optimal parabola is stored. Based on the resulting error map, candidates become points that are local extrema (minima) of such deviations (see more in C).

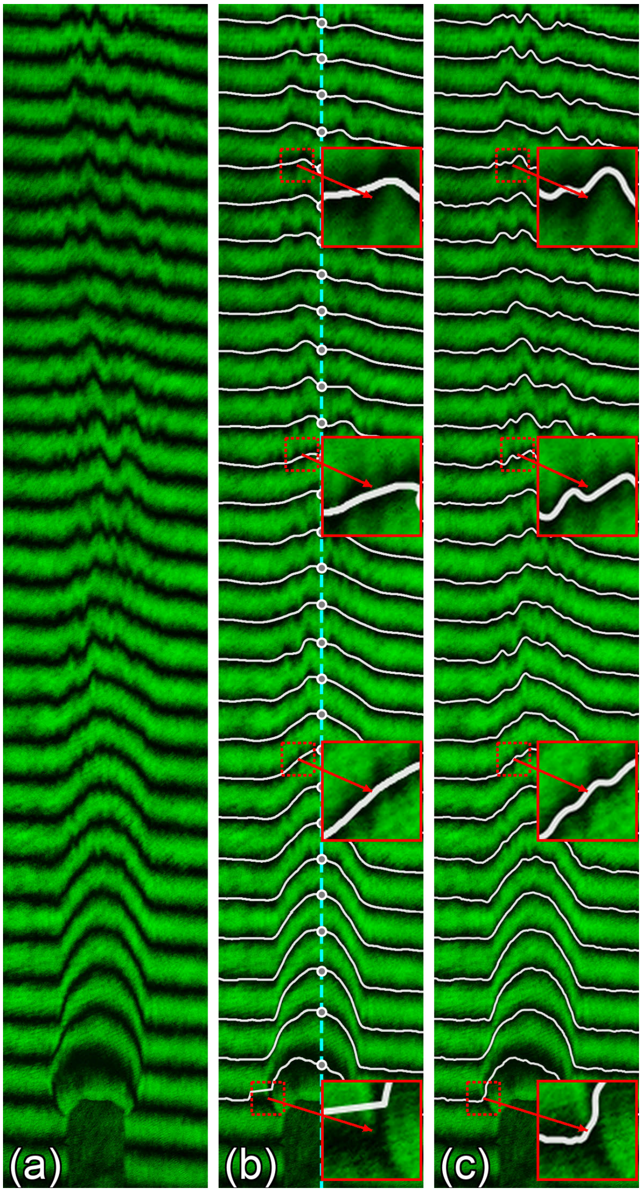

FIGURE 2. **(a) Experimental laser probing frame: shift interferogram of highly ionized plasma channel in atmospheric air. (b) The frame with white lines for pre-traced by the parabola method dark fringes with enlarged square insets. The dotted blue line highlights the starting points slice, and the starting points are marked with white circles. (c) The frame with white lines for SKIM-optimized dark fringes with enlarged square insets. The quantitative measurement of curve improvement is done using SKIM loss as a metric, which is described in detail in the IV-B Section and illustrated in the Figure 3(F).**

Further, the candidates are connected into **continuous lines**, with each line starting to be built from the first candidate point, the so-called base point. Depending on the specifics of the frame, base points can be selected from candidate points on one border of the frame (for example, the left vertical one) or points in a convenient slice through the center of the frame. In our work, the base points are selected in the central vertical slice of the frame (see Figure 2(b)), tracing goes both left and right, and then connects into a single line.

The tracing function iterates through the nearest neighboring points (with a step of 1 pixel) to the left, deviating further vertically up to the value of *max_search_distance*, determined empirically and equal to the maximum vertical jump of the line. If no candidate point is found in this area, the point with a step of 1 pixel to the left with the same ordinate is saved as the next point of the line. To the right, the trace is built similarly; then the right and left branches are connected into one black stripe.

To prevent fractures, after tracing, a one-dimensional Gaussian filter with σ_{Gauss}, in our case equal to 1 pixel, is applied to the ordinate of the line.

All dark fringes are **numbered** from top to bottom and stored as a list of geometric line objects (in our case, LineString from Shapely in Python). It will be useful to store the vertices of the line in coordinates (x, y) and to perform optimized functions: curve parameterization, calculation of the tangent at a line point, and uniform line discretization. Such representation will simplify further processing.

The result of this algorithm stage are the continuous black fringes identified in the frame, numbered from top to bottom, see Figure 2(b).

B. TUNING THE LINE POSITION

The line position tuning method is novel and offers an algorithm to improve the primary tracing of black lines. As will be shown in the Isophase Tuning subsection IV-H, it is also applicable and successful for correcting isophase positions.

Since the position of dark fringes determines the position of geometrically calculated isophases, which are then used to smooth the image brightness and calculate phases, incorrect calculation of dark lines critically affects the quality of the obtained result. Thus, additional computational and, consequently, time costs at this stage are fully justified to improve the quality of their calculation.

Since we are discussing quality, it is necessary to introduce a metric for the satisfactory construction of a black line. We propose this metric (subsection IV-B1) and explain the principle of its minimization (subsection IV-B2).

1) SMOOTHED KERNEL-BASED INTENSITY MEASURING FUNCTION

The original interferogram is noisy; the black fringes have non-zero width due to image pixelation; the diffraction is broadening of bands on the object. For all these reasons, the black fringe should not only pass through points with minimum brightness but also be surrounded by points with minimum brightness. The closer the points are to it, the lower the brightness is expected in them.

Let us introduce for each neighboring point a measure of its distance ρ - the shortest distance from the point to the initially constructed black curve. As the distance decreases, we expect a decrease in brightness.

The metric for the quality of black line placement, proposed by us as a loss function for optimizing the position of the curve, will be the integral of the pixel brightnesses near this curve with a kernel function $K(\rho)$. Empirical evidence - comparison of results with expert data - shows that the kernel function works more correctly due to its rapid decrease with increasing ρ than polynomial dependencies. At the same time, it remains computationally simple.

In discrete form, such a dependency is expressed as:

$$SKIM = \frac{\sum_{x,y \in U} I(x, y)K(\rho)}{N_{x,y \in U}}, \tag{1}$$

where $I(x, y)$ is the intensity of the pixel with coordinates (x, y), $K(\rho)$ is the Gaussian kernel $K(\rho) = \exp(-\frac{\rho^2}{2\sigma_{kernel}^2})$, U is the integration region, in our case all points with distance from the current black fringe no more than the boundary distance $3 * \sigma_{kernel}$, $N_{x,y \in U}$ is the number of points inside the integration region. σ_{kernel} should be chosen based on the specifics of the experimental series, it is approximately equal to the average half-width of the black line in pixels. The boundary distance should be chosen equal to the average half-width of the distance between the neighboring black fringes. The values of the kernel function inside the integral region are clearly displayed in Figure 3(E).

It is evident that the bottleneck in the computational complexity of this formula is the calculation of the shortest distances to the curve. It is aggravated by the need to enumerate curve variants. To quickly calculate such distances, it is proposed to use a K-dimensional-tree algorithm to find the nearest points on the curve, thus reducing the problem to a geometric search for the distance to a segment.

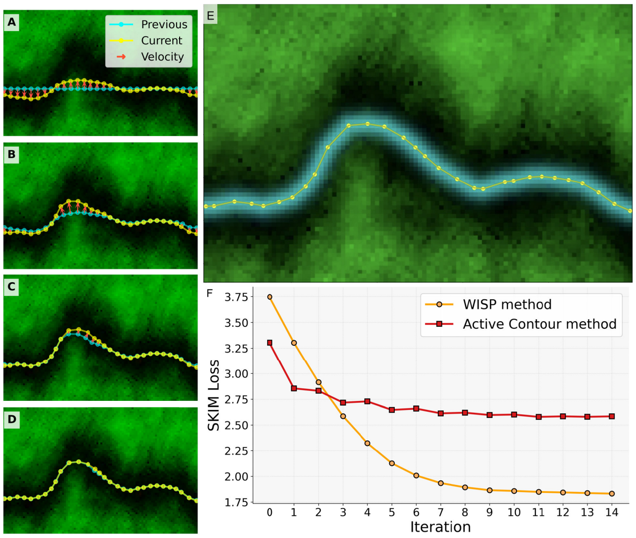

FIGURE 3. **The figure shows iterations of tuning of one dark line in the frame (A-D). The previous line position is marked with a blue line, the current - with yellow. The gradient forces are shown with red arrows. The integral region is colored in image E with blue gradations from the $K(\rho)$ kernel function value calculated for each pixel of the image. Image F demonstrates the behavior of SKIM Loss in the WISP method (orange line) and for the active contours method (red line).**

2) SKIM-FUNCTION MINIMIZATION

The SKIM-function minimization method employs the optimization principle of ML approaches, specifically gradient descent, to minimize the kernel integral in the minimization domain - the space between the curve under study and its neighbors.

The minimization method is iterative. At each iteration, for each point in the curve of the supposed black fringe, the gradient of the SKIM function is calculated relative to the shift of this point along the axes (x,y). Each point experiences a shift in the direction opposite to the gradient of the SKIM function, reducing the total loss $Loss = \sum_{x,y\in U} SKIM$ equal to the sum (1) for all points in the integral zone of the curve. The shift of the point in one iteration is controlled by a minimization parameter, the learning rate value, which in our case is a constant. Iterations are stopped when the change in loss per iteration does not exceed 0.1%.

For clarity, we demonstrate the algorithm's operation with an initially pre-traced black fringe (the first line from the top of the frame). The preliminary position of the black line is set as a straight horizontal line (see the blue line in Figure). A total of 16 iterations were performed before the loss converged; each fourth iteration is shown in Figure 3(A-D). The result of SKIM-optimization for all dark fringes in the frame can be seen in Figure 3(c).

The improvements in the quality of the fringe tracing are especially clearly visible on the lower dark fringe, in the near-electrode area. They are also significant in the upper filamented part of the object on the periphery, where spatially small fringe shifts are recorded with greater accuracy. Quantitatively, this is expressed in an improvement in SKIM characteristics by an average of 1.4 times.

3) VERIFICATION BY THE ACTIVE CONTOURS METHOD

To verify the loss function developed and its minimization method, the active contours method was also implemented in WISP. It has proven itself to be one of the most reliable methods for fitting black fringes ([37], [38]).

The method optimizes the position of the line to precisely follow the intensity minima using active contours. The contour energy is minimized, which consists of internal (regularization) and external forces (attraction to image features). The contour is updated at each iteration considering a combination of internal and external forces, corresponding to a numerical method. Note that a one-dimensional Gaussian filter was also applied to the curve to improve the method's stability. The balance between elasticity (α), rigidity (β), and external forces (γ) was optimized as described in the original article [37].

The Figure 3(F) shows the characteristic behavior of the SKIM loss function during WISP SKIM-minimization iterations, as well as the SKIM loss function as a metric for the active contours method.

Using SKIM-loss minimization, convergence is achieved more smoothly, and a significantly smaller loss is achieved, which means a higher (quantitatively 1.5 times) quality of tracing the black fringe relative to the active contours method.

C. GEOMETRICAL ISOPHASES CONSTRUCTION

The construction of connected lines (forming lines of presumed brightness preservation) in the first iteration of the calculation is performed in the simplest and computationally efficient way.

Given two adjacent black fringes, $\mathcal{L}_i$ and $\mathcal{L}_{i+1}$, we parameterize them as curves

$$\mathbf{x}_i : [0, 1] \to \mathbb{R}^2, \quad \mathbf{x}_{i+1} : [0, 1] \to \mathbb{R}^2.$$

Here it is necessary to involve the curve parametrization function with parameter M, which defines the number of isophases to construct between adjacent black fringes. The value M is recommended to be selected as the average ratio of the line width (the distance in pixels between undisturbed adjacent black fringes) to the characteristic longitudinal size of the object.

The coordinates of the interpolated isophase lines are then computed by linear interpolation between these parameterizations:

$$\begin{aligned} \mathbf{c}_i &= \mathbf{x}_i(t), \\ \mathbf{c}_{i+1} &= \mathbf{x}_{i+1}(t), \\ \mathbf{c}_\psi &= (1-\psi)\mathbf{c}_i + \psi\mathbf{c}_{i+1}, \\ \psi &\in \{\frac{1}{M+1}, \frac{2}{M+1}, \dots, \frac{M}{M+1}\}. \end{aligned} \tag{2}$$

where parameter t runs over the parameter domain [0, 1], and $\mathbf{c}_\psi$ represents the coordinates of the interpolated isophases between $\mathcal{L}_i$ and $\mathcal{L}_{i+1}$.

The result of this algorithm stage is the formation of continuous non-intersecting numbered isophases between black lines (see 4(a)). For visual clarity, here the parameter M is chosen equal to 5.

The analogues of the geometrical approach include other types of curve morphing [39]. However, practice [39] shows that with complex line geometry, this regularly causes the intersection of isophases, which is undesirable for the subsequent construction of phase gradient line segments, along which we will reconstruct the phase. Additionally, it is necessary to remember that this iteration is primary and therefore geometric simplification is advantageous due to its reliability.

D. LOCAL FRINGE DIRECTIONS FIELD

The calculation accuracy of the direction field is necessary for further anisotropic intensity smoothing.

The construction of the direction field is carried out on the basis of isophase lines, and their iterative refinement leads to the need to reconstruct the direction map at each iteration.

We need to extract N_{dir} equidistant points on the isophase line. N_{dir} should be chosen comparable to the frame width (approximately 2-3 times less than the number of dots on the dark fringe) so that points are placed frequently enough on the curves.

The algorithm then runs from the first to the last point of each dark fringe and isophase curve, calculating the local direction of the line using the formula:

$$\theta(x_i, y_i) = \arctan\left(\frac{y_{i+1} - y_i}{x_{i+1} - x_i}\right),$$

where $(x_i, y_i), (x_{i+1}, y_{i+1})$ are the coordinates of adjacent points on a line. This formula allows to avoid multiple-π uncertainty in the local direction of the fringe.

Thus, at each point of the isophase curves, including black lines, we know the angle of the local line direction. The next crucial step is the interpolation of the direction field in all other pixels of the frame.

An important aspect is the necessity of transitioning angle values to complex numbers:

$$z = \exp(1j \cdot \theta), z_{\text{real}} = \text{Re}(z), z_{\text{imag}} = \text{Im}(z) \tag{3}$$

and then separating interpolation in the real and imaginary domains z_{real}, z_{imag}. Working with interpolation in the domain of real angle values leads to angle jumps in the region of transition through 2π, as well as incorrect operation in areas of sharp jumps in the local slope angle of the line.

The result of this stage is the formation of a continuous direction field (see 4(b)).

E. SMOOTHING INTENSITY ALONG ISOPHASES

Calculating the local orientation field of the fringe, implemented in the previous stage of the algorithm, allows us to perform smart smoothing of the frame taking this information into account.

We use the smoothing method proposed in the work [40], which is dedicated to the application of the diffusion principle to image processing with significant anisotropy. This work demonstrates that, for continuous functions, the numerical iterative solution of the diffusion equation exists and is unique.

The diffusion equation is solved in the form:

$$\begin{cases} \dfrac{\partial I}{\partial t} = \text{div}\big(D\nabla I\big), \\[2ex] D = R_\theta \begin{bmatrix} \lambda_\parallel & 0 \\ 0 & \lambda_\perp \end{bmatrix} R_\theta^T, \\[2ex] R_\theta = \begin{bmatrix} \cos\theta & \sin\theta \\ -\sin\theta & \cos\theta \end{bmatrix}, \\[2ex] \nabla I = (\dfrac{\partial I}{\partial x}, \dfrac{\partial I}{\partial y}) \\[1ex] \theta = \theta(x, y), \quad I = I(x, y). \end{cases} \tag{4}$$

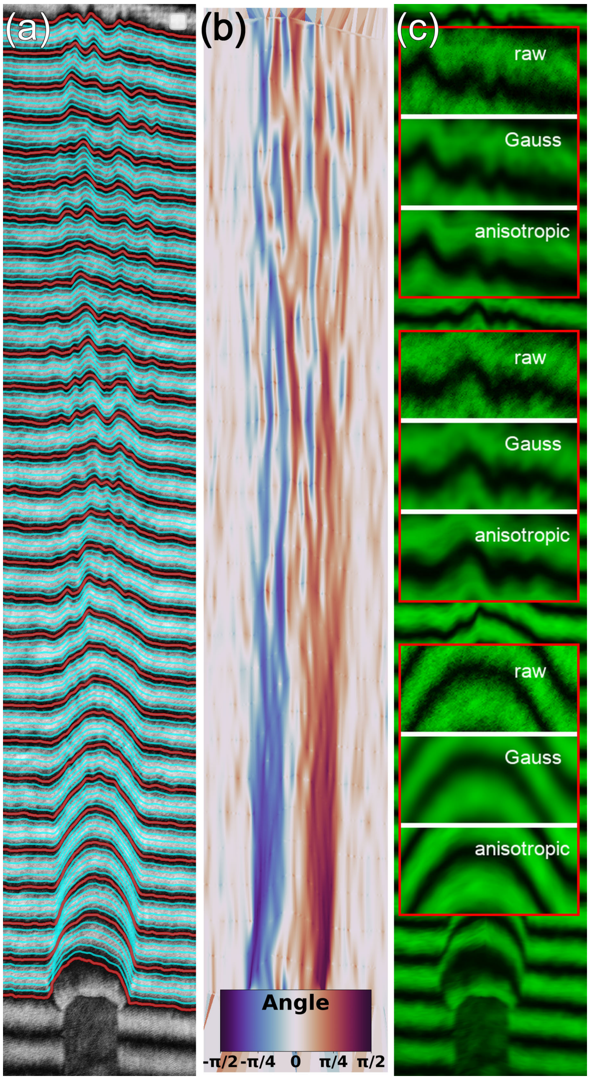

FIGURE 4. **(a) The frame with geometrically constructed isophases. Here the red lines reflect the dark fringes, the blue lines reflect the isophases. (b) The direction field – the local direction of the isophase for each point. Directions are plotted by color gradation. (c) Anisotropically smoothed image after first framework iteration. The enlarged insets in red show the differences between the raw experimental image (raw), the image smoothed with a Gaussian filter with a sigma of 3 (Gauss), and anisotropic smoothing with a sigma of 1.5 (anisotropic).**

Here t is the diffusion time (iterative parameter), D is the diffusion tensor, controlling the smoothing direction and strength; $\lambda_\parallel$ and $\lambda_\perp$ are the eigenvalues of D, representing diffusion coefficients along the parallel and perpendicular directions, respectively; R_θ is the rotation matrix aligning the diffusion tensor with the local image structure; $\theta(x, y)$ is the local orientation angle of the fringe pattern; ∇I is the image gradient vector; div denotes the divergence operator.

However, here we modify the form of the diffusion matrix by incorporating physical information about the formation of the interference pattern. Since the interference pattern implies the preservation of intensity along the isophase line, the diffusion matrix in our case is constructed not based on intensity gradients, as in the original work, but on the assumption that smoothing of the pattern should occur with maximal weighting in the direction of the angle θ, and minimal weighting in the direction normal to it. In the system of equations (4), $\lambda_\parallel$ is a numerical diffusion coefficient governing the rate of intensity propagation along the isophase direction, while $\lambda_{\perp}$ governs the rate of propagation normal to the isophase. In our case, these were empirically chosen as 0.3 and 0.005, respectively.

The iterative step δt was set at 0.1, and the number of iterations increases within each major workflow cycle from 20 to 100. Since we depart from the concept of the original method, we do not seek solution convergence; rather, our objective is to progressively enhance, with increasing information reliability (as the noise components are removed with increasing precision), the influence of intensity along the isophase on the global distribution of intensities along it.

The result of this algorithm stage is an interference pattern smoothed along the local line directions (see 4(c)). Note that this smoothing is performed independently for each iteration, relative to the original image, to avoid accumulation of smoothing errors and blurring of the phase pattern.

WISP anisotropic smoothing demonstrates maximum preservation of characteristic image profiles without smoothing the characteristic curve shapes caused by the probed object. It is more effective than a Gaussian filter in preserving line brightness while reducing noise.

F. GRADIENT LINE FORMATION

The gradient line formation function implements an algorithm for constructing phase gradient lines perpendicular to isophases, with division into zones between neighboring dark fringes. Each zone is processed independently.

For each zone, starting points for constructing gradient lines are evenly distributed on the one of boundary lines (black fringe). The number of points is set by the parameter *n_gradients_per_zone* and should be comparable to the frame width (*width*/3 in our case).

For each starting point, a phase gradient line is traced. Tracing is carried out as follows: from the current point, a projection is made onto the next isophase in the zone. The found projection point becomes the next point of the gradient line, and iterations continue until the second boundary of the zone is reached (see Figure 5). For a more balanced distribution of gradient curves in each zone, even starting points are taken on the upper black fringe of the zone, odd ones - on the lower one.

In Figure 6(a), gradient lines are depicted as blue lines.

G. PHASE UNWRAPPING

This part of the framework implements an algorithm to reconstruct the phase distribution from an interference pattern, using data about dark fringes and phase gradient lines. The algorithm is based on a combination of local phase recovery and global interpolation, taking into account zones between dark fringes.

For each phase gradient line in the zone between neighboring dark fringes, points are evenly selected. The intensity of the interference pattern is measured at these points. The phase is locally recovered through the arccosine of the normalized intensity:

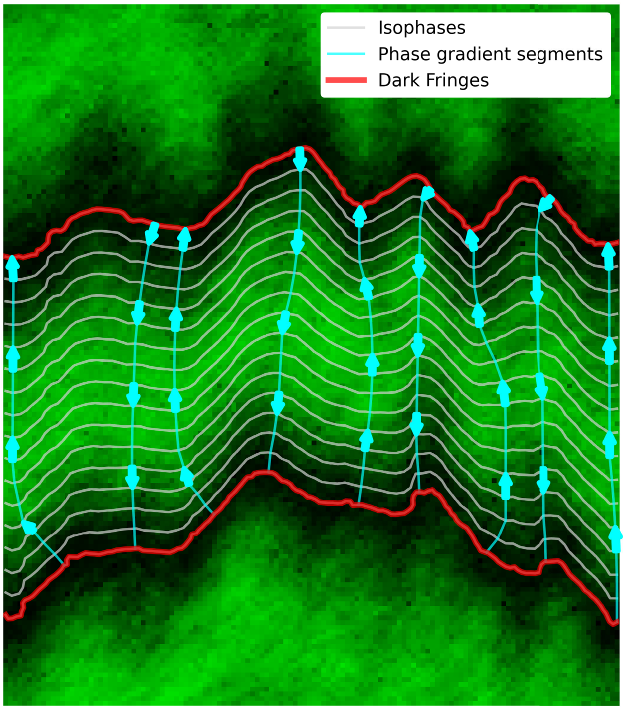

FIGURE 5. The figure shows one zone between the neighbor black fringes (shown by red lines), where a series of gradient lines (blue lines) are obtained from the reference isophases (shown by gray lines). The projection directions are shown by blue arrows.

$$\phi(x, y) = \arccos\left(\frac{I(x, y) - \bar{I}}{max_{(x,y)\in Z}\left(I(x, y) - \bar{I}\right)}\right),$$

$$\bar{I} = \frac{1}{|Z|} sum_{(x,y)\in Z} I(x, y), \tag{5}$$

where Z is the geometrical zone between neighboring black fringes, $I(x, y)$ is the intensity in (x, y) pixel of the gradient line in zone Z.

Each zone between the black fringes corresponds to a phase change of 2π. For the k-th zone, $2\pi k$ is added to the locally reconstructed phase, ensuring smooth phase stitching between zones.

The points belonging to dark fringes are fixed with a phase value of $\pi + 2\pi k$, where k is the zone number. This corresponds to the intensity minima in the interference pattern.

All reconstructed phase values (including points of gradient lines and dark fringes) are used to build a smooth phase field throughout the image. Linear interpolation is applied to obtain a continuous phase distribution.

Thus, the method uses information about dark fringes and gradient lines, which allows correct phase reconstruction even in complex cases with inhomogeneities. By adding $2\pi k$ to the phase in each zone, the continuity of the reconstructed phase field is ensured, and stitching is not required. The phase

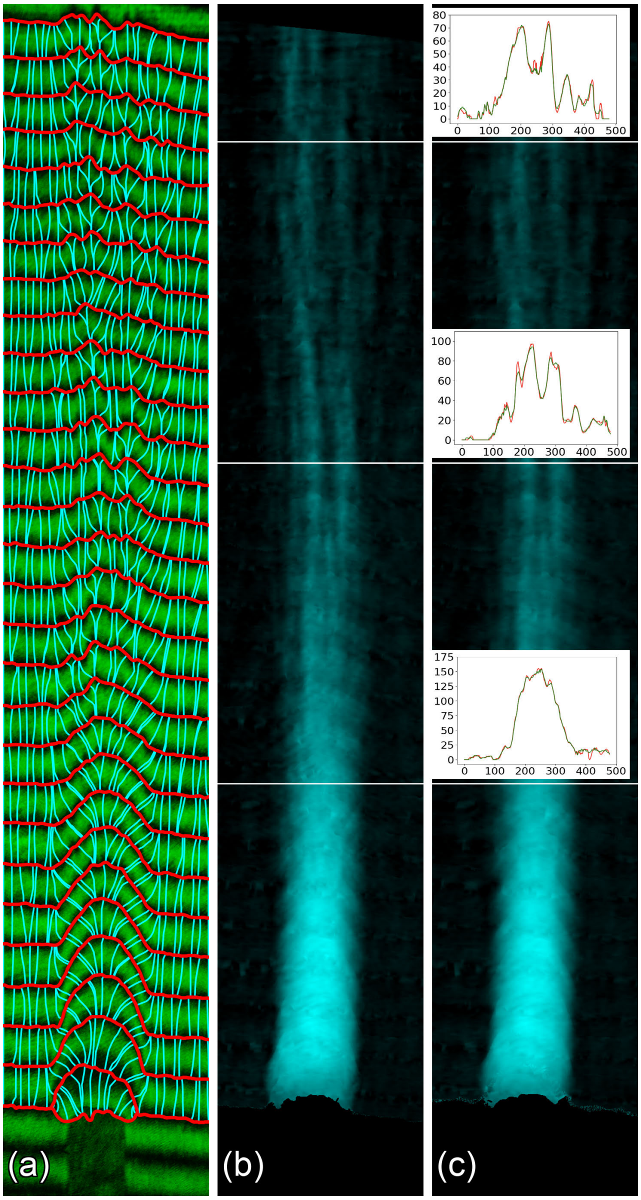

FIGURE 6. **(a) The frame with gradient lines (figure shows a limited number of lines for clarity). Here the red lines reflect the dark fringes, the blue lines reflect the gradients. (b) Phase after 1 iteration. (c) Phase after 5 iterations. The phase shift distributions by slices (white lines) in Figs. (b) and (c) are shown by the red curve for the 1st iteration and by the green curve for the 5th iteration on all 3 subgraphs.**

is normalized to the interval $[-\pi, \pi]$ in each zone, but with a shift of $2\pi k$ to ensure continuity.

Phase unwrapping beyond the outer black fringes

A separate problem is phase restoration beyond the uppermost and lowermost black fringes registered in the frame. Even if there are no significant parts of the object there, correct phase restoration beyond the boundary fringes is crucial for correct processing of further framework iterations.

Since it is impossible to restore correct and complete isophases outside the boundary dark fringes, it is proposed to extrapolate gradient lines in these zones by straight lines (see Figure 7(a) where the method is shown on a fragment of a frame as an example), restoring the phase distribution on the gradient line as described above. The phase unwrapping in the remaining points is achieved by interpolation (see Figure 7(b)).

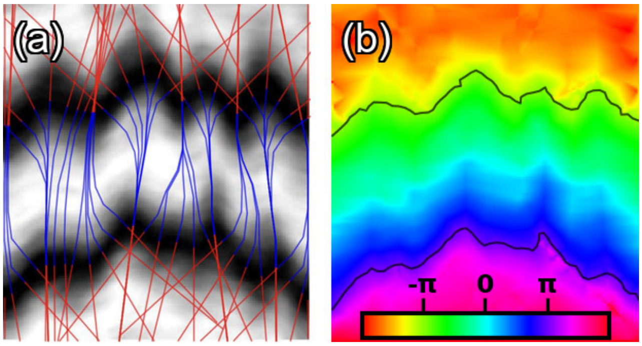

FIGURE 7. **(a) Extrapolation of gradient lines (dark blue lines) beyond the boundary dark fringes is shown by red lines. (b) Phase unwrapping in and out of boundary fringes. The phase values are reflected by the color gradient, dark fringes are marked as black lines.**

The result of the phase unwrapping block is a continuous 2-dimensional phase pattern (see Figure 8(c)).

Phase shift calculation

For maximum visual clarity of the result, we will take into account that a shift interferogram is being studied.To restore the phase shift $\delta\phi$ on the object, it is necessary to process in a similar way the interference frame recorded without the object, with unperturbed lines.

In the figure, we show a frame without an object (Figure 8(a)), its phase pattern obtained after the first (Figure 8(b)) and after the fifth iteration (Figure 8(b)). The result of subtracting the phase distribution, restored from the frame without an object, from the phase scan of the frame with an object, is shown in the Figure 6(b), which most clearly displays the result of the framework cycle, giving the possibility of visually assessing the quality of processing.

H. TUNING DARK FRINGES AND ISOPHASE POSITIONS

Since we have complete information about the presumed phases in the frame, updating the positions of dark fringes and isophases (including dark fringes, except for the upper and lower boundary ones) can be performed much more accurately than their initial construction.

We believe that ideally the black lines should run along the constant phase line:

$$\phi_k = -\pi + 2\pi k, \quad k \in [1, D-2],$$

where D is the total number of dark fringes, k is the fringe (and the associated zone) number.

As intermediate isophases are evenly distributed between the phases of the zone boundary dark fringes, they are presumed to have phase:

$$\phi_{k,m} = -\pi + 2\pi k + m \cdot \Delta\phi, \quad \Delta\phi = \frac{2\pi}{M+1},$$

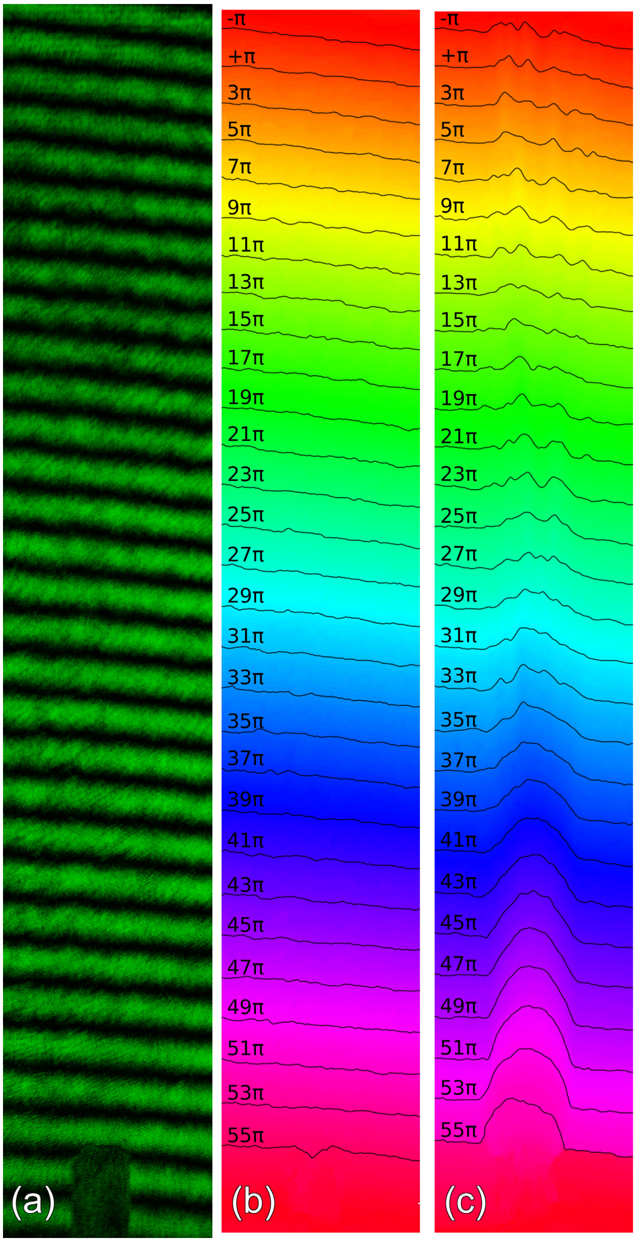

FIGURE 8. **(a) The interference frame recorded without the object. (b) Phase pattern for frame without object after 1 iteration.(c) Phase pattern for frame with object after 1 iteration. The phase values in (b) and (c) are reflected by the color gradient, dark fringes are marked as black lines.**

where $m \in [1, M]$, m is the isophase number in the zone k.

The tracing of a new SKIM-tunned line, whether it is a black fringe or an intermediate isophase, is performed using the SKIM-function minimization method (IV-B2). Let us explain here how it can be used for tracing any isophase in general form when a presumed phase map is available.

For each target phase $\phi_{k,m}$, a map of the difference function $F = (\phi - \phi_{k,m})^2$ is constructed, whose minima correspond to the desired line.

Then, the dark fringe tracing algorithm with minimization of the brightness SKIM-function is applied to the resulting difference function map, calculated on the map of function F. Gradient descent is implemented until the loss function is convergent.

I. STOPPING CRITERION

At this stage, we make the most reliable check of the result: we compare the smoothed experimental data $I(x, y)$, normalized to the interval [0; 2], with the $1 + \cos(\phi(x, y))$ function, realized in interferometry. Mathematically, this is expressed by the formula:

$$\text{RMS} = \sqrt{\frac{\sum_{x,y}\left(I(x,y) - (1 + \cos(\phi(x,y)))\right)^2}{N_{x,y}}}. \quad (6)$$

If the change in the last 2 iterations in this difference is no more than 0,1 percent of its absolute value, the algorithm returns the two-dimensional phase distribution obtained in the last iteration. In addition, the algorithm returns the numerical error of phase reconstruction based on the comparison of the model (obtained on the basis of the phase distribution) interferogram with the experimental one. Otherwise, the next cycle (IV-D- IV-I) is started.

In our case, it took a number of 5 iterations to achieve the required quality. The result of the algorithm was a phase shift distribution that is shown in Figure 6(b). The RMS value in the first iteration was equal to 0.156, in the fifth iteration it was equal to 0.113.

The numerical improvement of the metric, comparing the unwrapped phase pattern with the experiment, can be visually seen by comparing the results of iterations 1 and 5 in Figure 6. Since the reduction in noise and the increase in phase shift accuracy are difficult to discern with the eye, we have added subgraphs that demonstrate the obvious difference. The background noise is minimized, all objects are restored to the maximum resolution boundary of the experimental setup.

It is evident that with the increase in the number of iterations, random intensity bursts associated with the imperfection of the experimental image (noise and artifacts) are suppressed, without bringing amplitude and spatial distortions to the supporting structures of the object. Green lines preserve the curvature in the object area, while getting rid of random noise intensity bursts, even fairly smooth ones, noticeable on the red curves.

V. NOISE ROBUSTNESS

For a comprehensive analysis of WISP results, we present a widely used [9] research method of the framework's robustness to image noise. We added Gaussian white noise to the original image. The ratio of the white noise amplitude to the image brightness amplitude varied from 0 to 0.5 with a step of 0.05. The resulting noisy images are shown in the Figure 9, where image (A) is a noise-free frame, and (B-K) are noisy images with increasing noise amplitude.

The framework was launched without additional manual fine-tuning of the coefficients on the previous parameters.

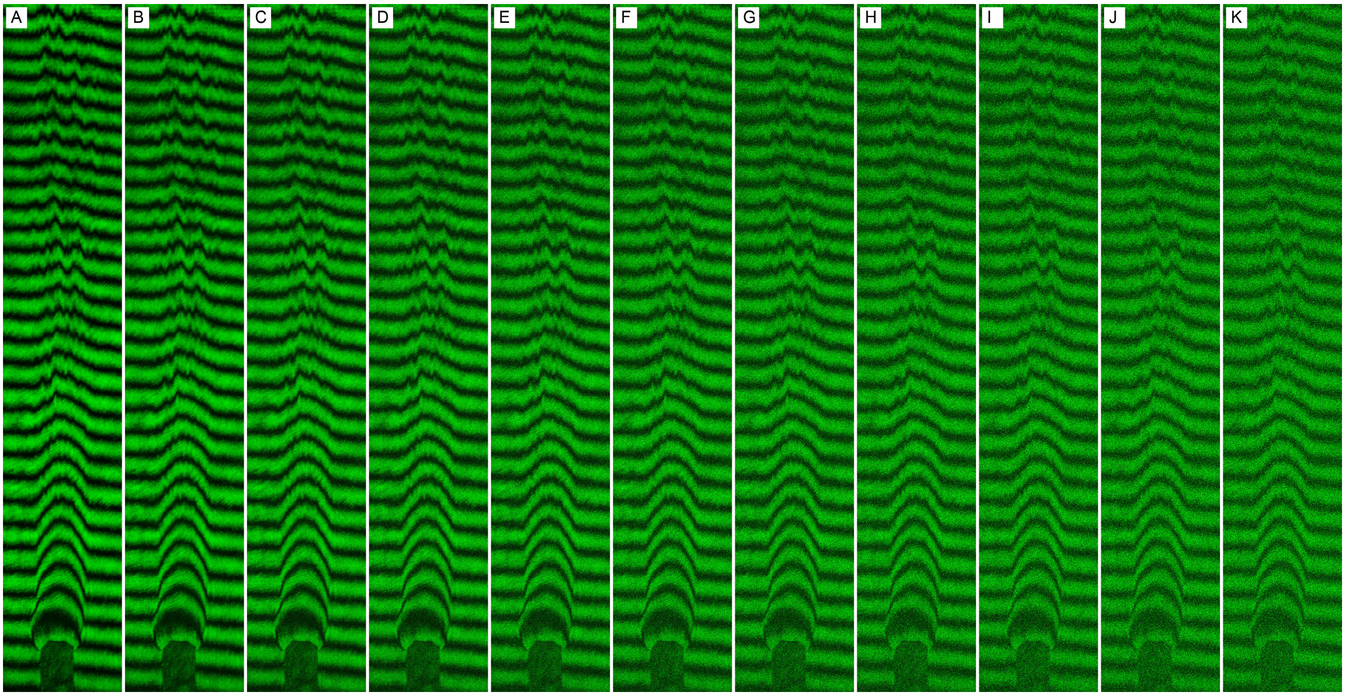

FIGURE 9. (A) The original image. (B-K) Images with increasing ratio of the amplitude of the introduced white Gaussian noise to the amplitude of the original image brightness from 0.05 to 0.5 with a step of 0.05.

TABLE 1. Dependence of RMS error and number of iterations required for convergence on noise level.

Noise level	RMS	Number of iterations
0	0.113	5
0.05	0.329	6
0.10	0.385	7
0.15	0.403	7
0.20	0.411	8
0.25	0.420	8
0.30	0.443	8
0.35	0.449	9
0.40	0.463	9
0.45	0.471	10
0.50	0.495	10

We measured the RMS achieved during convergence, as well as the iteration number at which convergence was achieved. The results obtained are reflected in the Table 1 and in the Figure 10.

The results show high resistance to noise on the RMS metric, since when the noise increases to half the amplitude of the original pattern, the accuracy changes no faster than linearly. The increase in error is primarily due to the increase in the noise of the original pattern, with which the interference transformation of the obtained smooth phase pattern is compared on the RMS metric.

Increasing the number of iterations to 10 (twice as much as for the noise-free image) is not critical in terms of increasing the computational time.

The obtained results demonstrate the robustness of the proposed framework to high noise levels.

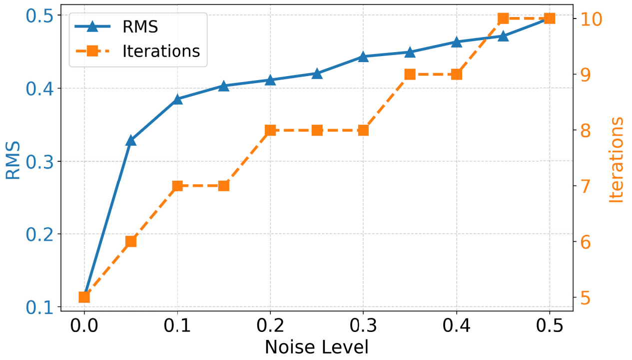

FIGURE 10. Graph of the dependence of the achieved RMS and the number of iteration at which it was achieved on the ratio of the amplitude of the introduced noise to the amplitude of the brightness of the original image.

VI. COMPARISON WITH ALTERNATIVE METHODS

In this section, we compare the proposed method with several popular approaches on phase unwrapping, proven (see [9]) their high precision of results and noise robustness, while having accessible reproducibility. Our baselines are: the path-dependent method RFNP [6], [7], path-independent methods - TIE and ITIE [8], PM [1], EAPM [2], and the deep neural network DCNN [9] without refinement (final corrections of incorrect phase values), so that the algorithms compete on equal terms.

The investigated baseline methods, published between 2017 and 2021, represent relatively contemporary approaches in the field. To the best of the authors' knowledge, more recent techniques, predominantly deep learning-based methodologies, either lack publicly accessible implementations or datasets necessary for independent validation, or focus on other peculiarities of phase images for restoration.

To compare the results with these methods, we processed the unnoised and noisy samples presented in the paper (Figures 5 and 6 in work [9]) with the WISP framework, having previously divided them into sections, for each of which a starting points slice for pre-tracing is uniquely determined, and also excluded the center of closed line to meet our assumptions. The noised image has added Gaussian white noise on the wrapped phase map, the standard deviation is set to 1.0, as in work [9].

The metric on which the results will be compared is the most popular for processing phase patterns, RMSD. However, unlike formula for RMS(6), we will compare the reconstructed phase with the true phase $\phi^{real}(x, y)$, and not the interference pattern of the reconstructed phase with the experiment, as proposed in our work. This is due to the fact that for reference comparison we have the opportunity to use a model of true phase, which is unknown when processing experimental images.

$$\mathrm{RMSD} = \sqrt{\frac{\sum_{x,y}\left(\phi(x, y) - \phi^{real}(x, y)\right)^2}{N_{x,y}}} \tag{7}$$

Performance metrics are reported in Table 2. Computations were performed on Intel Core i7-10750H (6 cores, 12 threads) with NVIDIA GTX 1650 Ti GPU. We present the average computation time for both types of images.

TABLE 2. Performance comparison of phase reconstruction methods on clear and noised images with processing times.

Method	Clear image	Noised image	Processing time (sec)
RFNP [6]	**3.5e-13**	3.62	2.76
TIE [8]	0.90	6.6	0.19
ITIE [8]	0.20	4.21	0.42
PM [1]	1.00	1.02	0.71
EAPM [2]	0.86	0.89	2.87
DCNN [9]	0.56	0.68	0.18
WISP	**0.18**	**0.41**	5.12

The highest quality of the path-dependent method on a noise-free image is compensated by a significant drop in quality on a noisy image. Path-independent methods demonstrate less noise robustness and worse accuracy metrics. The neural network method outperforms good results on a noisy image. PM and EAPM show stable results on clean and noisy images, intermediate with other baselines for clean images and close to the best for noisy images. WISP demonstrates a result that loses only to RFNP, which is tuned for ideal image quality, in accuracy on a noise-free object, and provides maximum robustness to noise.

Practice shows that the accuracy at the first WISP iteration is often sufficient to achieve accuracy (7) exceeding that of PM and EAPM, and its convergence is achieved by 5-10 iterations.

It can be seen that phase values obtained with the WISP framework show more robust results than functional methods and DCNN. The fundamental absence of smoothing error accumulation, taking into account the local direction of the fringes in smoothing, the iterative correction of the fringes and isophases, and the use of additional information about the physical background of the experiment allow WISP to reconstruct the noise-free picture and unwrap the phase with greater accuracy than other algorithms.

The disadvantage of the presented framework is the longer computation time compared to the other methods. However, it should be mentioned that in the task of processing unique experimental frames, the duration of the computations is not critical, since the purpose of research is the accuracy and reliability of the results obtained.

VII. CONCLUSION

The WISP framework has been developed - an iterative phase unwrapping system that integrates:

- initial phase estimation via the PM;
- dynamic refinement of isophases and field vectors (directional and gradient);
- anisotropic smoothing along local pattern direction;
- precision-controlled termination criteria based on phase reconstruction accuracy.

A novel method for quantative assessment and tuning the position of the fringe closest to the given phase with the author's loss function and the gradient descent method with its optimization has been developed, which has a significant advantage in accuracy compared to the popular active contour method solution.

The strengths of the WISP framework are the highest precision of the result, noise robustness and the complete absence of the need for fine manual adjustment.

The results of the framework that implements the proposed algorithms and produces reliable output data are presented. Comparison was made with well-known widely used methods, reproducible and focused on a problem statement close to that described in the article. The relatively high accuracy and robustness of the framework was shown.

For reproducibility of the data obtained in the scientific community, the code is available in link.

APPENDIX A
ALGORITHMIC PSEUDOCODE

For greater clarity, we provide an algorithmic diagram explaining which results of each method are used in subsequent stages.

APPENDIX B
KEY SYMBOLS AND NOTATIONS

Table 3 summarizes all key mathematical notations and parameters used in the article. Spatial coordinates (x, y) are typically measured in pixels.

Algorithm 1 Algorithmic Pseudocode for WISP

```
Input: Interferogram $I(x, y)$
Output: Reconstructed phase $\phi(x, y)$
fringes $\leftarrow$ PreTracing($I$)
fringes* $\leftarrow$ SKIMTuning(fringes, $I$)
isophases $\leftarrow$ GeometricIsophases(fringes*)
for $k \leftarrow 1$ to $max\_iterations$ do
    $D \leftarrow$ CalcDirField(fringes*, isophases)
    $I_{\text{smooth}} \leftarrow$ AnisotropicSmoothing($I$, $D$)
    $G \leftarrow$ GradientLines(fringes*, isophases)
    $\phi \leftarrow$ PhaseUnwrapping($I_{\text{smooth}}$, $G$)
    if $\|I -$ InterferenceFunction$(\phi)\| < \epsilon$ then
        break
    end
    fringes* $\leftarrow$ SKIMTuning(fringes*, $I$)
    isophases $\leftarrow$ SKIMTuning($\phi$)
end
return $\phi$
```

TABLE 3. Key symbols and notations.

Symbol	Quantity	Section/Equation
$\phi(x, y)$	Phase distribution	Sec. III-A, Eq. (1)
$\nabla\phi$	Phase gradient vector	Sec. III-A
$\mathcal{L}_i$	i-th dark fringe curve	Sec. IV-A
$\mathbf{c}_\psi$	Isophase coordinates	Sec. IV-C, Eq. (2)
$\theta(x, y)$	Local fringe direction	Sec. IV-D
$K(\rho)$	Gaussian kernel function	Sec. IV-B, Eq. (1)
σ_{kernel}	Kernel width parameter	Sec. IV-B
D	Diffusion tensor	Sec. IV-E, Eq. (3)
$\lambda_\parallel$	Parallel diffusion coefficient	Sec. IV-E
$\lambda_\perp$	Perpendicular diffusion coefficient	Sec. IV-E
R_θ	Rotation matrix	Sec. IV-E, Eq. (3)
$I(x, y)$	Intensity pattern	Throughout
I_{smooth}	Anisotropically smoothed intensity	Sec. IV-E
G	Gradient lines set	Sec. IV-F
M	Number of isophases per zone	Sec. IV-C
N_{dir}	Direction field sampling points	Sec. IV-D
$N_{x,y}$	Pixel count in integration region	Sec. IV-B
$SKIM$	Smoothed Kernel-based Intensity Metric	Sec. IV-B, Eq. (1)
ρ	Distance to nearest curve point	Sec. IV-B
U	Integration region ($\rho \leq 3\sigma_{kernel}$)	Sec. IV-B
$\delta\phi$	Phase shift	Sec. IV-G
ϵ	Convergence threshold	Sec. IV-H

APPENDIX C
PM FRINGE TRACING: CANDIDATE POINTS

Candidate points for intensity minima of the recorded interference pattern are identified as follows.

Since the intensity varies approximately as a cosine between fringes and can be locally approximated by a parabola near an extremum, we focus only on points close to the parabola's vertex. This helps exclude false local extrema caused by noise and optical artifacts.

Consider a point A suspected to be an extremum in the intensity profile. Near an extremum, the intensity variation for the neighboring points around A can be approximated by a quadratic function: $I_i \approx a * i^2 + b * i + c$, where a, b, c are the unknown coefficients, i is the distance between A and the neighboring point in pixels.

To find the best fit parabola, we minimize the sum of squared residuals $\chi^2 = \sum_i (I_i - a*i^2 - b*i - c)^2$ by parameters a, b, c. Finding the points which are the local minima of χ^2, candidate extrema are found. The sign of a_0 classifies the extremum type: if $a_0 > 0$, point A indicates a minimum.

ACKNOWLEDGMENT

The work was supported by a grant for research centers in the field of artificial intelligence provided by the Ministry of Economic Development of the RF under the subsidy agreement (agreement identifier 000000C313925P3Q0002) with National Research Nuclear University MEPhI No. 70-2023-001309. *(Timofey F. Khirianov and Ilya Makarov are co-first authors.)*

REFERENCES

[1] A. I. Khirianova, E. V. Parkevich, M. A. Medvedev, T. F. Khirianov, and A. S. Selyukov, "Algorithm of interferogram Tracing. I. the parabola method: Pros and cons," *J. Russian Laser Res.*, vol. 42, no. 1, pp. 25–31, Jan. 2021, doi: 10.1007/s10946-020-09926-1.

[2] A. I. Khirianova, E. V. Parkevich, M. A. Medvedev, T. F. Khirianov, and A. S. Selyukov, "Algorithm of interferogram Tracing. II. fringes with negative curvature and extended approach to their processing," *J. Russian Laser Res.*, vol. 42, no. 2, pp. 161–170, Mar. 2021, doi: 10.1007/s10946-021-09945-6.

[3] E. V. Parkevich, S. I. Tkachenko, A. V. Agafonov, A. R. Mingaleev, V. M. Romanova, T. A. Shelkovenko, and S. A. Pikuz, "Study of the prebreakdown stage of a gas discharge in a diode with point cathode by laser probing," *J. Experim. Theor. Phys.*, vol. 124, no. 4, pp. 531–539, Apr. 2017, doi: 10.1134/s1063776117030074.

[4] E. V. Parkevich, M. A. Medvedev, A. I. Khirianova, G. V. Ivanenkov, A. V. Agafonov, A. S. Selyukov, A. R. Mingaleev, T. A. Shelkovenko, and S. A. Pikuz, "Investigation of a near-electrode plasma formed in the atmospheric discharge with employment of picosecond laser probing," *J. Russian Laser Res.*, vol. 40, no. 1, pp. 56–63, Jan. 2019, doi: 10.1007/s10946-019-09769-5.

[5] E. V. Parkevich, M. A. Medvedev, A. I. Khirianova, G. V. Ivanenkov, A. S. Selyukov, A. V. Agafonov, K. V. Shpakov, and A. V. Oginov, "Extremely fast formation of anode spots in an atmospheric discharge points to a fundamental ultrafast breakdown mechanism," *Plasma Sources Sci. Technol.*, vol. 28, no. 12, Dec. 2019, Art. no. 125007, doi: 10.1088/1361-6595/ab518e.

[6] M. A. Herráez, D. R. Burton, M. J. Lalor, and M. A. Gdeisat, "Fast two-dimensional phase-unwrapping algorithm based on sorting by reliability following a noncontinuous path," *Appl. Opt.*, vol. 41, no. 35, pp. 7437–7444, Dec. 2002, doi: 10.1364/ao.41.007437.

[7] M. F. Kasim. (2017). *Fast 2D Phase Unwrapping Implementation in MATLAB*. [Online]. Available: https://github.com/mfkasim91/unwrap/

[8] J. Martinez-Carranza, K. Falaggis, and T. Kozacki, "Fast and accurate phase-unwrapping algorithm based on the transport of intensity equation," *Appl. Opt.*, vol. 56, no. 25, pp. 7079–7088, Sep. 2017, doi: 10.1364/ao.56.007079.

[9] T. Zhang, S. Jiang, Z. Zhao, K. Dixit, X. Zhou, J. Hou, Y. Zhang, and C. Yan, "Rapid and robust two-dimensional phase unwrapping via deep learning," *Opt. Exp.*, vol. 27, no. 16, pp. 23173–23185, Aug. 2019, doi: 10.1364/oe.27.023173.

[10] J. H. Bruning, D. R. Herriott, J. E. Gallagher, D. P. Rosenfeld, A. D. White, and D. J. Brangaccio, "Digital wavefront measuring interferometer for testing optical surfaces and lenses," *Appl. Opt.*, vol. 13, no. 11, pp. 2693–2703, Nov. 1974, doi: 10.1364/ao.13.002693.

[11] D. Malacara-Herndez and Z. Malacara-Hernndez, *Handbook of Optical Design*. Boca Raton, FL, USA: CRC Press, 2017, ch. 1, doi: 10.1201/b13894.

[12] S. Zhang, "High-speed 3D shape measurement with structured light methods: A review," *Opt. Lasers Eng.*, vol. 106, pp. 119–131, Jul. 2018, doi: 10.1016/j.optlaseng.2018.02.017.

[13] R. Smythe and R. Moore, "Instantaneous phase measuring interferometry," *Opt. Eng.*, vol. 23, no. 4, Aug. 1984, Art. no. 234361, doi: 10.1117/12.7973301.

[14] D. G. Abdelsalam, B. Yao, P. Gao, J. Min, and R. Guo, "Single-shot parallel four-step phase shifting using on-axis Fizeau interferometry," *Appl. Opt.*, vol. 51, no. 20, pp. 4891–4895, Jul. 2012, doi: 10.1364/ao.51.004891.

[15] K. Qian, "Two-dimensional windowed Fourier frames for noise reduction in fringe pattern analysis," *Opt. Eng.*, vol. 44, no. 7, Jul. 2005, Art. no. 075601, doi: 10.1117/1.1948107.

[16] Q. Kemao, "Two-dimensional windowed Fourier transform for fringe pattern analysis: Principles, applications and implementations," *Opt. Lasers Eng.*, vol. 45, no. 2, pp. 304–317, Feb. 2007, doi: 10.1016/j.optlaseng.2005.10.012.

[17] M. Jiang, W. Chen, Z. Zheng, and M. Zhong, "Fringe pattern analysis by S-transform," *Opt. Commun.*, vol. 285, no. 3, pp. 209–217, Feb. 2012, doi: 10.1016/j.optcom.2011.09.015.

[18] M. Takeda, "Spatial-carrier fringe-pattern analysis and its applications to precision interferometry and profilometry: An overview," *Ind. Metrology*, vol. 1, no. 2, pp. 79–99, Jun. 1990, doi: 10.1016/0921-5956(90)80019-r.

[19] M. A. Saville, A. J. Hamilton, and J. E. Caplinger, "An automated 2-D line-shift measurement from smoothed and leveled diagnostic interferometric images of exploded-wire plasma," *IEEE Trans. Plasma Sci.*, vol. 51, no. 12, pp. 3570–3578, Dec. 2023, doi: 10.1109/TPS.2023.3341258.

[20] S. Kim and Y.-S. Kim, "Two-dimensional phase unwrapping using wavelet transform," *Electron. Lett.*, vol. 38, no. 1, pp. 19–20, Jan. 2002, doi: 10.1049/el:20020007.

[21] J. Chu, Y. Jiang, Q. Li, and D. Zhao, "Interferogram processing with wavelet analysis and spectrogram reconstruction," *Proc. SPIE*, vol. 4221, pp. 91–94, Oct. 2000, doi: 10.1117/12.403916.

[22] P. Wang, M. Shan, and Z. Yin, "Denoising of smart-phone based fringe projection image using curvelet transform," in *Proc. 3rd Int. Conf. Digit. Signal Process.*, Feb. 2019, pp. 7–11, doi: 10.1145/3316551.3316559.

[23] C. Wang and F. Da, "Phase demodulation using adaptive windowed Fourier transform based on Hilbert–Huang transform," *Opt. Exp.*, vol. 20, no. 16, pp. 18459–18469, Jul. 2012, doi: 10.1364/oe.20.018459.

[24] M. Trusiak, Ł. Służewski, and K. Patorski, "Single shot fringe pattern phase demodulation using Hilbert–Huang transform aided by the principal component analysis," *Opt. Exp.*, vol. 24, no. 4, pp. 4221–4238, Feb. 2016, doi: 10.1364/oe.24.004221.

[25] S. M. A. Bhuiyan, R. R. Adhami, and J. F. Khan, "Fast and adaptive bidimensional empirical mode decomposition using order-statistics filter based envelope estimation," *EURASIP J. Adv. Signal Process.*, vol. 2008, no. 1, Dec. 2008, Art. no. 728356, doi: 10.1155/2008/728356.

[26] K. Wang, Y. Li, Q. Kemao, J. Di, and J. Zhao, "One-step robust deep learning phase unwrapping," *Opt. Exp.*, vol. 27, no. 10, pp. 15100–15115, May 2019, doi: 10.1364/oe.27.015100.

[27] K. Yan, Y. Yu, T. Sun, A. Asundi, and Q. Kemao, "Wrapped phase denoising using convolutional neural networks," *Opt. Lasers Eng.*, vol. 128, May 2020, Art. no. 105999, doi: 10.1016/j.optlaseng.2019.105999.

[28] S. Feng, Q. Chen, G. Gu, T. Tao, L. Zhang, Y. Hu, W. Yin, and C. Zuo, "Fringe pattern analysis using deep learning," *Adv. Photon.*, vol. 1, no. 2, p. 1, Feb. 2019, doi: 10.1117/1.ap.1.2.025001.

[29] Y. Kuang, J. Li, F. Liu, Y. Wu, and R. Zhang, "Fast and high precision phase recovery technology of single-shot ineterferogram based on depth convolution neural network," *J. Opt.*, vol. 26, no. 2, Feb. 2024, Art. no. 025701, doi: 10.1088/2040-8986/ad1589.

[30] Y. Kuang, F. Liu, Y. Liu, X. Chen, Y. Wu, and R. Zhang, "Correction of spurious phase sign in single closed-fringe demodulation using transformer based swin-ResUnet," *Opt. Laser Technol.*, vol. 168, Jan. 2024, Art. no. 109952.

[31] M. Servin, J. L. Marroquin, and F. J. Cuevas, "Demodulation of a single interferogram by use of a two-dimensional regularized phase-tracking technique," *Appl. Opt.*, vol. 36, no. 19, pp. 4540–4548, Jul. 1997, doi: 10.1364/ao.36.004540.

[32] R. Legarda-Saenz and M. Rivera, "Fast half-quadratic regularized phase tracking for nonnormalized fringe patterns," *J. Opt. Soc. Amer. A, Opt. Image Sci.*, vol. 23, no. 11, pp. 2724–2731, Nov. 2006, doi: 10.1364/josaa.23.002724.

[33] C. Tian, Y. Yang, D. Liu, Y. Luo, and Y. Zhuo, "Demodulation of a single complex fringe interferogram with a path-independent regularized phase-tracking technique," *Appl. Opt.*, vol. 49, no. 2, pp. 170–179, Jan. 2010, doi: 10.1364/ao.49.000170.

[34] C. A. Balanis, *Advanced Engineering Electromagnetics*, 2nd ed., Hoboken, NJ, USA: Wiley, 2012.

[35] I. Gurov and M. Volkov, "Fringe evaluation and phase unwrapping of complicated fringe patterns by the data-dependent fringe processing method," *IEEE Trans. Instrum. Meas.*, vol. 55, no. 5, pp. 1634–1640, Oct. 2006, doi: 10.1109/TIM.2006.880276.

[36] E. V. Parkevich, G. V. Ivanenkov, M. A. Medvedev, A. I. Khirianova, A. S. Selyukov, A. V. Agafonov, A. R. Mingaleev, T. A. Shelkovenko, and S. A. Pikuz, "Mechanisms responsible for the initiation of a fast breakdown in an atmospheric discharge," *Plasma Sources Sci. Technol.*, vol. 27, no. 11, Nov. 2018, Art. no. 11LT01, doi: 10.1088/1361-6595/aaebdb.

[37] M. Kass, A. Witkin, and D. Terzopoulos, "Snakes: Active contour models," *Int. J. Comput. Vis.*, vol. 1, no. 4, pp. 321–331, Jan. 1988, doi: 10.1007/bf00133570.

[38] T. F. Chan and L. A. Vese, "Active contours without edges," *IEEE Trans. Image Process.*, vol. 10, no. 2, pp. 266–277, Feb. 2001, doi: 10.1109/83.902291.

[39] G. Wolberg, "Image morphing: A survey," *Vis. Comput.*, vol. 14, nos. 8–9, pp. 360–372, Dec. 1998, doi: 10.1007/s003710050148.

[40] J. Weickert, *Anisotropic Diffusion in Image Processing*. Stuttgart, Germany: Teubner, 1998, pp. 55–62.

TIMOFEY F. KHIRIANOV received the Specialist degree in physics and mathematics from Moscow Institute of Physics and Technology, Moscow, Russia.

Since 2006, he has been a Lecturer with Moscow Institute of Physics and Technology. Since 2020, he has been a Lecturer with Lomonosov Moscow State University, Moscow. Since 2021, he has been a Researcher with the Lebedev Physical Institute of the Russian Academy of Sciences, Moscow.

ALEKSANDRA I. KHIRIANOVA received the Specialist degree in physics and mathematics and the Ph.D. degree in physics and mathematics from Moscow Institute of Physics and Technology, Moscow, Russia.

Since 2018, she has been a Researcher with the Lebedev Physical Institute of the Russian Academy of Sciences, Moscow. Since 2024, she has been a Senior Researcher with the Institute of Artificial Intelligence, Lomonosov Moscow State University, Moscow.

EGOR V. PARKEVICH received the Specialist degree in physics and mathematics from Moscow Institute of Physics and Technology, Moscow, Russia, and the Ph.D. degree in physics and mathematics from the Lebedev Physical Institute of the Russian Academy of Sciences, Moscow.

Since 2015, he has been a Researcher with the Lebedev Physical Institute of the Russian Academy of Sciences, where he is currently the Head of the Laboratory of Laser Diagnostics of Plasma Structures.

ILYA MAKAROV received the Specialist degree in mathematics from Lomonosov Moscow State University, Moscow, Russia, and the Ph.D. degree in computer science from the University of Ljubljana, Ljubljana, Slovenia.

Since 2011, he has been a Lecturer with the School of Data Analysis and Artificial Intelligence, HSE University, where he was the School Deputy Head, from 2012 to 2016. He was the Program Director of the Big Data Academy MADE-VK and a Researcher with the Samsung-PDMI Joint AI Center, St. Petersburg Department, V. A. Steklov Mathematical Institute, Russian Academy of Sciences, Saint Petersburg, Russia. He is currently an Associate Professor and a Senior Research Fellow. He is also a Senior Research Fellow with the Artificial Intelligence Research Institute (AIRI), Moscow, where he leads the research in industrial AI. He became the Head of the AI Research Center and the Data Science Tech Master's Program in NLP, National University of Science and Technology MISIS.

• • •